Magnetic Resonance in Medicine 65:702–714 (2011)

Simultaneously Driven Linear and Nonlinear Spatial Encoding Fields in MRI

Daniel Gallichan,[1]* Chris. A. Cocosco,[1] Andrew Dewdney,[2] Gerrit Schultz,[1] Anna Welz,[1] Jürgen Hennig,[1] and Maxim Zaitsev[1]

Spatial encoding in MRI is conventionally achieved by the application of switchable linear encoding fields. The general concept of the recently introduced PatLoc (Parallel Imaging Technique using Localized Gradients) encoding is to use nonlinear fields to achieve spatial encoding. Relaxing the requirement that the encoding fields must be linear may lead to improved gradient performance or reduced peripheral nerve stimulation. In this work, a custom-built insert coil capable of generating two independent quadratic encoding fields was driven with high-performance amplifiers within a clinical MR system. In combination with the three linear encoding fields, the combined hardware is capable of independently manipulating five spatial encoding fields. With the linear *z*-gradient used for slice-selection, there remain four separate channels to encode a 2D-image. To compare trajectories of such multidimensional encoding, the concept of a local *k*-space is developed. Through simulations, reconstructions using six gradient-encoding strategies were compared, including Cartesian encoding separately or simultaneously on both PatLoc and linear gradients as well as two versions of a radial-based in/out trajectory. Corresponding experiments confirmed that such multidimensional encoding is practically achievable and demonstrated that the new radial-based trajectory offers the PatLoc property of variable spatial resolution while maintaining finite resolution across the entire field-of-view. Magn Reson Med 65:702–714, 2011. © 2010 Wiley-Liss, Inc.

Key words: nonlinear spatial encoding; quadratic fields; PatLoc; Non-Fourier encoding

INTRODUCTION

Spatial encoding in MRI is conventionally achieved by the application of linear field gradients, aligned with the principal Cartesian axes of the magnet, which can be switched rapidly and independently. Physiological limitations in the switching rate of such fields have led to the development of alternative geometries for creating linear encoding fields (1), with the aim of reducing the maximal dB/dt by making the gradient fields more local. The general concept of PatLoc (Parallel Imaging Technique using Localized Gradients) (2,3) is to relax the requirement that the spatial encoding magnetic fields (SEMs) must vary linearly across the field-of-view (FoV) by introducing SEMs exhibiting spatial variation of higher order than standard linear gradients. Parallel imaging technology enables MR imaging with spatially ambiguous encoding fields and, once understood, this additional degree of spatial encoding freedom may lead to improved gradient performance or reduced peripheral nerve stimulation.

Low amplitude nonlinear SEMs in the form of a paraboloid of revolution (4) (or "bowl-shape") and a hyperbolic paraboloid (5) (or "saddle-shape") have previously been used to introduce a small additional nonlinear phase distribution to the object. The additional phase imparts a spatially dependent dispersion of the *k*-space signal, thereby reducing the dynamic range required of the analog-to-digital converter. In these cases, the nonlinear SEM was deliberately weak compared with the linear SEMs to minimize distortion during Fourier reconstruction.

In principle, encoding can be achieved with arbitrary combinations of linear and nonlinear SEMs. However, typical MRI hardware is capable of driving up to three spatially dependent magnetic field gradients simultaneously. Using a custom-built ultra-low field (0.0192 T) system, a nonlinear SEM has been used directly in conjunction with linear SEMs to produce Fresnel encoding as an alternative to Fourier encoding (6). A preliminary result demonstrating experimental data collected with nonlinear SEMs in simultaneous combination with conventional linear SEMs using a commercially available MR system is presented in (7). In that study, an SEM in the form of a paraboloid of revolution was manipulated using hardware designed for real-time shimming, concurrent to the conventional gradients. Real-time shimming amplifiers are typically designed to a much lower specification than gradient amplifiers with respect to power and rise-time performance.

In this work, we present data collected on a modified clinical MRI system which has been fitted with a duplicate set of gradient amplifiers, thereby being capable of driving up to six independent SEMs with high power and fast switching rates. Using a custom-built gradient insert coil (8,9) to generate two hyperbolic paraboloid fields, we were able to acquire data with simultaneous manipulation of the linear and curvilinear SEMs.

A further consideration when using simultaneous linear and curvilinear encoding is how to design the "trajectory" along which to drive the increased number of encoding channels. For this study, we considered the case of 2D imaging (using the *z*-gradient for slice selection), with four encoding fields (linear *x*, linear *y*, curvilinear *a*, and curvilinear *b*) which can be manipulated independently to provide the in-plane spatial encoding.

[1]Department of Radiology, University Medical Center Freiburg, Freiburg, Germany.

[2]Siemens Healthcare, Erlangen, Germany.

*Correspondence to: Daniel Gallichan, D.Phil., Department of Radiology, Medical Physics, University Medical Center Freiburg, Breisacher Str. 60a, 79106 Freiburg, Germany. E-mail: daniel.gallichan@uniklinik-freiburg.de

Received 20 June 2010; revised 3 September 2010; accepted 14 September 2010.

DOI 10.1002/mrm.22672

Published online 30 November 2010 in Wiley Online Library (wileyonlinelibrary.com).

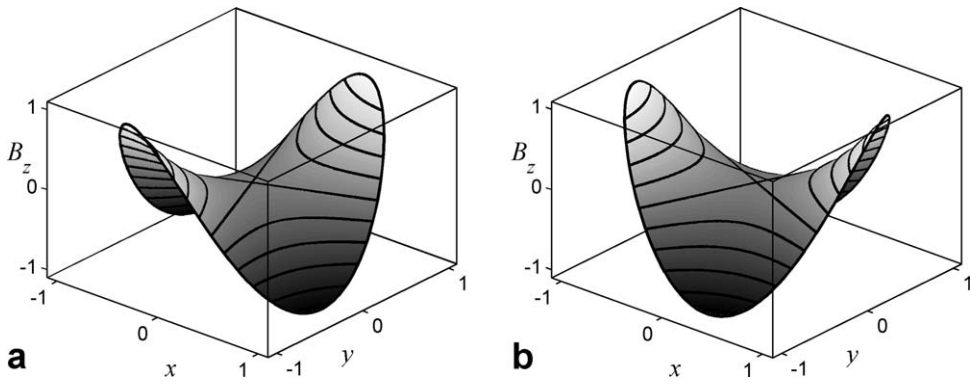

FIG. 1. The two curvilinear PatLoc encoding fields, SEM_a and SEM_b, used here in addition to the standard linear encoding. Both fields are close approximations to an ideal hyperbolic paraboloid, and are rotated 45° to each other. All axes are shown in normalized units.

We investigate how such four-dimensional trajectories can be compared and optimized.

THEORY

It has been shown previously that, neglecting relaxation effects, the signal s from RF receive channel α can be generalized to include encoding fields beyond simple linear gradients (3):

$$s_\alpha(\mathbf{k}) = \int_V m(\mathbf{x}) c_\alpha(\mathbf{x}) e^{i\mathbf{k}^T \psi(\mathbf{x})} d\mathbf{x} \quad [1]$$

where $m(\mathbf{x})$ is the magnetization at position $\mathbf{x}$, $c_\alpha(\mathbf{x})$ is the sensitivity of coil α at position $\mathbf{x}$, and $\boldsymbol{\psi}(\mathbf{x})$ is a multidimensional function representing all the gradient encoding fields. $\mathbf{k}$ is a vector of the same length as the number of gradient encoding fields, describing the net gradient moment of each field. To match our available hardware, within this manuscript, we consider encoding with four fields—the conventional linear x and y gradients, along with two additional curvilinear fields, SEM_a and SEM_b. Both curvilinear SEMs have the form of a hyperbolic paraboloid, and they are rotated by 45° with respect to each other to be orthogonal. These fields are depicted in Fig. 1, but it should be noted that the theory presented here is valid for arbitrary SEMs.

To perform a measurement, we necessarily order the samples of $\mathbf{k}$ with respect to time, t, so for the four encoding fields considered in our experiment we can rewrite the phase term in Eq. 1 as:

$$\mathbf{k}^T(t)\boldsymbol{\psi}(\mathbf{x}) = k_x(t)x + k_y(t)y + k_a(t)\psi_a(\mathbf{x}) + k_b(t)\psi_b(\mathbf{x}) \quad [2]$$

where $k_x(t)$ and $k_y(t)$ are equivalent to the familiar k-space coordinates in 2D (i.e., $k_x(t) = \gamma \int_0^t G_x(t')dt'$, where γ is the gyromagnetic ratio) and $k_a(t)$ and $k_b(t)$ are new k-space coordinates describing the amount of phase encoding due to the fields SEM_a and SEM_b at time t. $\psi_a(\mathbf{x})$ and $\psi_b(\mathbf{x})$ are appropriately scaled versions of the fields SEM_a and SEM_b. We can then define $k_a(t) = \beta \int_0^t I_a(t')dt'$, where I_a is the current running through the windings of the coil which generates SEM_a and β is a scaling constant. The variables $k_b(t)$ and $\psi_b(\mathbf{x})$ are defined in the equivalent manner for SEM_b.

The Concept of "Local *k*-Space"

In conventional MRI, with linear gradients, the coverage of the k-space formed by the components k_x and k_y (and k_z for 3D acquisitions) for a particular readout trajectory carries information regarding the properties of the images produced from the trajectory. For a full Cartesian coverage of k-space: $\Delta\mathbf{k}$ corresponds to the inverse of the FoV of the acquisition, and the maximum k values correspond to the resolution of the acquisition. The image resolution is constant across the object because the linear gradients result in the spatial derivative of the accumulated phase being independent of location. The FoV is also a spatially independent property for the same reason. When encoding with curvilinear SEMs in addition to the linear gradients, however, the image resolution and FoV are no longer spatially independent. Here, we introduce a local k-space, a concept that allows some interpretation of the imaging properties of a particular trajectory with higher-order spatial encoding.

For encoding with linear gradients only, the accumulated phase, ϕ, at location $\mathbf{x}$ and time t can be written as a function of the gradient history:

$$\phi(\mathbf{x}, t) = \gamma \int_0^t \mathbf{x} \cdot \mathbf{G}(t')dt' \quad [3]$$

where $\mathbf{G}(t)$ is the vector describing the applied linear gradient field at time t. This can lead to an alternative expression for $\mathbf{k}(t)$ (10):

$$\mathbf{k}(t) = \nabla\phi(\mathbf{x}, t). \quad [4]$$

This shows that an alternative way to conceptualize k-space is that it reflects the local spatial derivative of the accumulated phase at location $\mathbf{x}$. When using linear encoding, k-space is spatially independent because the first derivative of the phase is independent of $\mathbf{x}$ (so $\mathbf{x}$ does not appear on the left side of Eq. 4). However, when encoding with nonlinear fields, the local spatial derivative of the phase becomes location dependent, and we can no longer remove the spatial dependence from $\mathbf{k}$. We, therefore, define a local k-vector field, $\mathbf{k}_{\text{loc}}(\mathbf{x},t)$ as:

$$\mathbf{k}_{\text{loc}}(\mathbf{x}, t) = \nabla\phi(\mathbf{x}, t). \quad [5]$$

This definition of a local k-space is consistent with how the term has previously been used to describe local

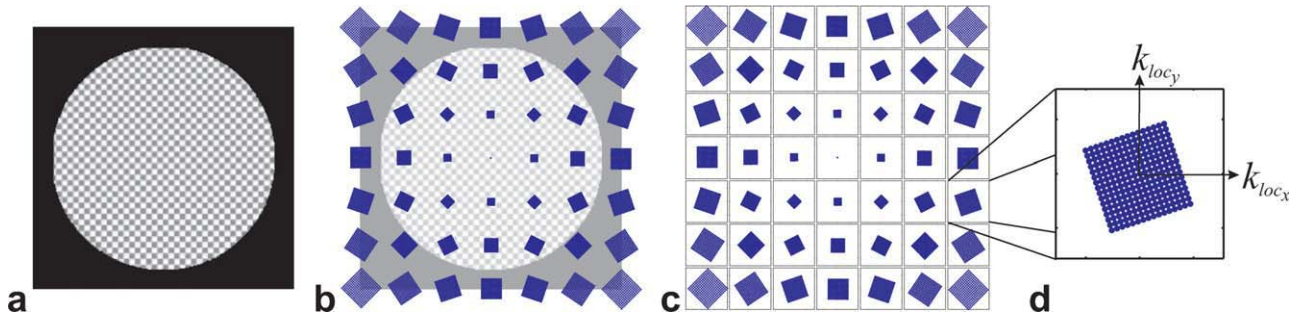

FIG. 2. Interpreting local *k*-space grids. **a**: The digital phantom used for simulations. **b**: A 7 × 7 grid of local *k*-space diagrams for the Pure PatLoc Cartesian trajectory, overlaid on the each corresponding location across the phantom. **c**: The same local *k*-space grid without the underlay. **d**: A zoom of one of the local *k*-space plots, indicating how each individual plot on the local *k*-space grid shows the *x* and *y* components of $\boldsymbol{k}_{\text{loc}}$ for the trajectory at a particular location in space.

changes in the effective trajectory for conventional imaging in the presence of B0 inhomogeneities (11–13).

Whereas the conventional *k*-space representation for a 2D acquisition with linear gradients can easily be visualized on a single 2D graph, the spatial variation of local *k*-space means that a 2D acquisition is represented fully by a unique version of such a 2D graph for every location **x**. If we can assume that our SEMs are slowly varying with **x**, we can instead choose a subset of locations to plot local 2D graphs for, allowing the observer to infer the behavior of the graphs in the regions in between. Figure 2 demonstrates this method of visualizing the local *k*-space. A simulated object is shown in Fig. 2a,b is overlaid with a 7 × 7 grid of local *k*-space plots for a Cartesian trajectory of the PatLoc quadratic encoding fields (k_a,k_b) with no use of linear gradients (k_x,k_y). The same grid is shown without the underlay of the phantom in Fig. 2c, and the zoomed plot in Fig. 2d shows that each individual local *k*-space plot indicates the values of k_{loc_x} and k_{loc_y} for a single position in the object. The number of points in the trajectory has been restricted to 16 × 16 (as for all local *k*-space plots in this article) to allow easier visualization.

MATERIALS AND METHODS

Encoding Trajectories

In this work, we compare six encoding trajectories, which make different use of the linear and quadratic encoding fields. Diagrams of the linear (k_x,k_y)-space and the quadratic (k_a,k_b)-space for each of the trajectories are shown on the left-most side of Figs. 3 and 4, where the color of the circles indicates the order of the samples during each readout line (see legend), and the size of the circles indicates the order in which the readout lines are acquired (largest to smallest).

- *Trajectory 1: Pure Linear Cartesian.* The simplest trajectory we considered in this work is the "conventional" approach of following a line-by-line Cartesian trajectory using only the linear gradients.
- *Trajectory 2: Pure PatLoc Cartesian.* The next trajectory we considered was to encode using a line-by-line trajectory using only the quadratic PatLoc encoding fields (i.e., Cartesian in (k_a,k_b)-space instead of (k_x,k_y)-space).
- *Trajectory 3: Dual Cartesian.* The simplest combined trajectory we considered (i.e., encoding using both

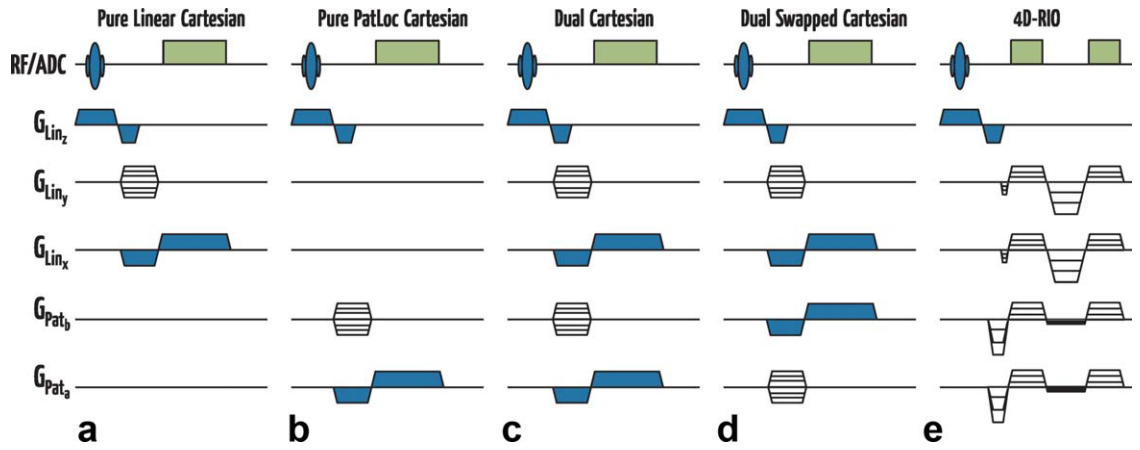

FIG. 3. Pulse sequence diagrams for (**a**) Pure Linear Cartesian, (**b**) Pure Patloc Cartesian, (**c**) Dual Cartesian, (**d**) Dual Swapped Cartesian (PatLoc channels *a* and *b* are swapped compared to (c)) and (**e**) 4D-RIO trajectories. The striped regions in (a–d) represent phase encoding. In (e) there is no phase encoding and the striped regions indicate the rotation of the radial-based trajectory.

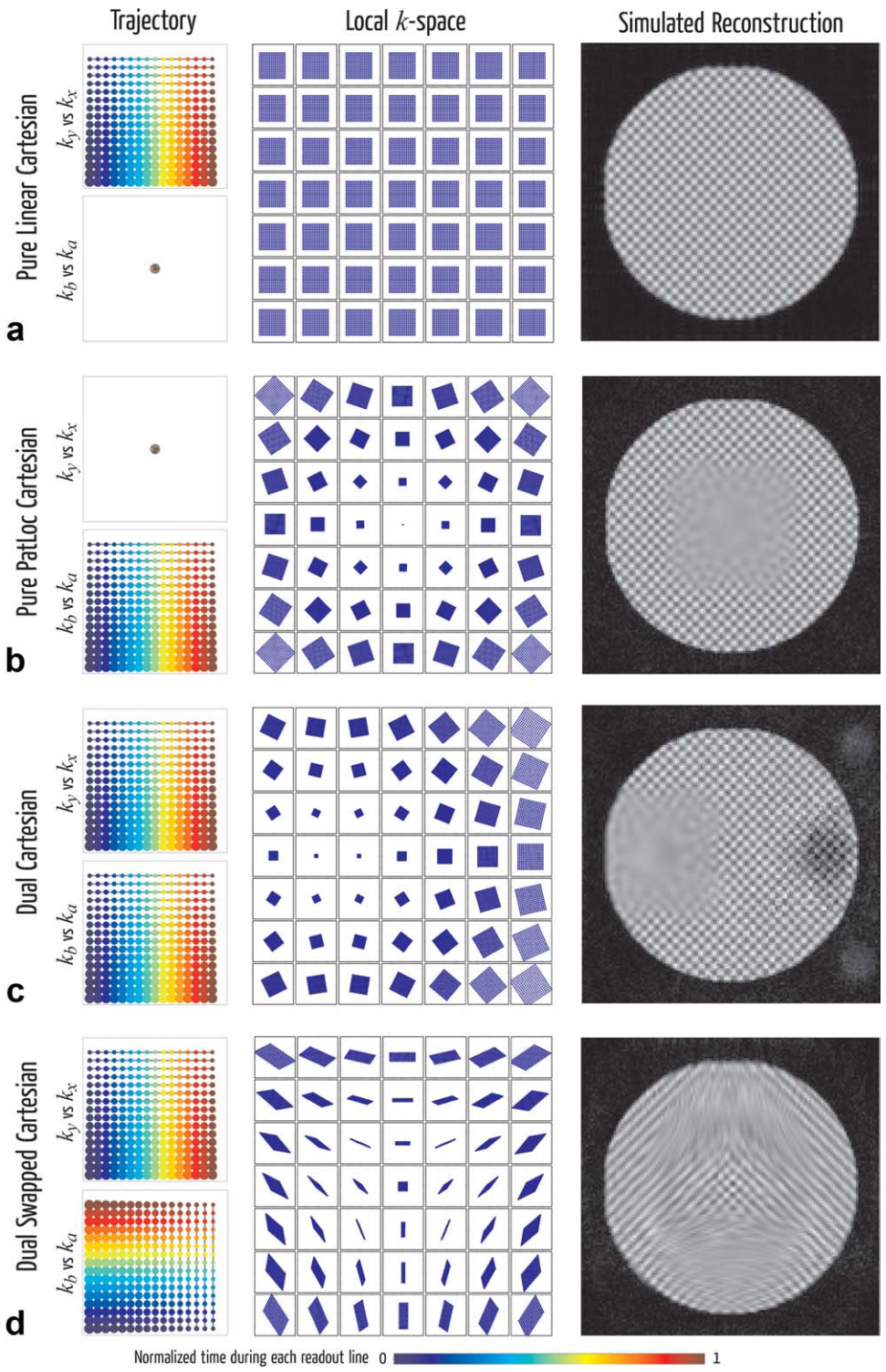

FIG. 4. Trajectory diagrams, 7 × 7 grid local *k*-space diagrams and reconstructed simulated data for (**a**) Pure Linear Cartesian, (**b**) Pure PatLoc Cartesian, (**c**) Dual Cartesian, and (**d**) Dual Swapped Cartesian trajectories. For trajectories, the color of each circle represents the normalized time per readout line and the size of each circle represents the order of the acquisition of the readout lines (largest to smallest). [Color figure can be viewed in the online issue, which is available at wileyonlinelibrary.com.]

the linear and PatLoc gradients simultaneously) was to use a Cartesian line-by-line trajectory in both the linear (k_x,k_y)-space and the quadratic (k_a,k_b)-space.

- *Trajectory 4: Dual Swapped Cartesian.* Identical to the Dual Cartesian trajectory, but with the role of the two quadratic encoding fields swapped (i.e., SEM_a used for phase-encoding instead of SEM_b).
- *Trajectory 5: 4D-RIO.* A radial-based trajectory where both the linear encoding and the quadratic PatLoc encoding follow separate radial trajectories with the same angle of advance between spokes (i.e., $\Delta\theta_{Lin} = \Delta\theta_{Pat}$). However, the timing is staggered such that when the center of the linear (k_x,k_y)-space is being traversed, the edge of the quadratic (k_a,k_b)-space is reached, and vice versa. We refer to this trajectory as 4-Dimensional Radial In/Out (4D-RIO).
- *Trajectory 6: 4D-RIO^2.* Identical to the 4D-RIO trajectory, but with different angles of advance for the

linear encoding compared to the quadratic encoding: $\Delta\theta_{Lin} = -2\Delta\theta_{Pat}$

Software Simulation

To approximate the RF coil sensitivity profiles of an eight-channel receive coil (to match our available hardware), the Biot-Savart Law was used to calculate the expected field surrounding a set of eight current loops arranged in a circle. For easier interpretation of simulations, we chose to define $\psi_a(\mathbf{x}) = x^2 - y^2$ and $\psi_b(\mathbf{x}) = 2xy$, although our physical coils are rotated by $\sim$22.5° from the main axis. This does not affect the validity of the simulations, however, as any effective rotation can be achieved by linear combinations of the encoding fields.

All simulations and image reconstruction were performed using Matlab (The Mathworks, Natick, MA) running on a desktop computer (2.66 GHz dual-core processor). The digital phantom (a checkerboard multiplied by a circular mask) was generated on a 256 × 256 Cartesian grid and Fourier filtered using a 2D Hamming window to remove the very high spatial frequency components. Simulated data were then generated for each trajectory using a total of 64 × 64 sampling points for eight RF coils (the profiles of which were simulated using the Biot-Savart Law). Normally distributed complex noise was added with a standard deviation of 5% of the mean absolute signal. These data were then reconstructed onto a 128 × 128 Cartesian grid, stopping after 50 CG iterations as described in the following section. Each CG iteration took $\sim$30 sec for each trajectory.

Image Reconstruction

With the 4D *k*-vector as defined in Eq. 2 being used to encode a 2D object (or a 2D slice through a 3D object), we can, in general, no longer use the Fourier transform directly to reconstruct the data. Instead we rewrite Eq. 1 in matrix form:

$$\mathbf{s} = \mathbf{E}\mathbf{m} \quad [6]$$

where $\mathbf{s}$ is column vector of data samples with $N_c N_\kappa$ rows (= no. of RF coils × no. of data samples), $\mathbf{m}$ is the column vector of magnetization values which represents the image of our object (i.e., what we wish to reconstruct) with N_ρ rows and $\mathbf{E}$ is the $N_c N_\kappa \times N_\rho$ encoding matrix, which incorporates both the phase terms resulting from the *k*-vector and the RF coil sensitivity values represented in Eq. 1 by $c_\alpha(\mathbf{x})$. A conjugate gradient (CG) technique was then be used to iterate toward $\mathbf{E}^\dagger\mathbf{s}$ (where $\mathbf{E}^\dagger$ represents the pseudoinverse of $\mathbf{E}$), in a similar manner to that described in (14) (although it should be noted that in our case the Fourier transform can still not be directly incorporated to speed up reconstruction time). Using the CG method avoids the need to explicitly calculate the pseudoinverse of $\mathbf{E}$, a process which can be very time consuming due to its large size. A further advantage of using such an iterative method is the "built-in" regularization (15). Direct use of the explicit calculation of $\mathbf{E}^\dagger\mathbf{s}$ is likely to result in overamplification of noise terms, whereas with the CG method, regularization can be introduced by stopping the process after a certain number of iterations. Choosing the appropriate number of iterations to use is, therefore, a compromise between bias (not enough iterations) and noise amplification (too many iterations).

Depending on the number of data points acquired and the desired resolution of the reconstructed image, the matrix $\mathbf{E}$ may quickly become too large to store in working memory on a typical desktop PC (e.g., for 128 × 128 data points, eight RF coils, reconstructed onto a grid of 128 × 128 voxels, $\mathbf{E}$ would require >17 Gb of memory to be stored as complex values at single precision). In such cases, the matrix $\mathbf{E}$ can be processed row-by-row for each iteration. This makes the reconstruction considerably slower, but massively reduces the memory requirements.

Hardware

All experiments were conducted on a 3T clinical imaging system (MAGNETOM Trio Tim, Siemens Healthcare, Erlangen, Germany) fitted with a custom-built gradient insert-coil designed to generate two encoding fields. The geometry of fields closely approximates a hyperbolic paraboloid (or second order), and orthogonality was achieved by rotating one of the fields by 45° with respect to the other (see Fig. 1). We refer to these two PatLoc curvilinear encoding fields as SEM_a and SEM_b. A PatLoc arrangement of this kind has been previously described in (8,9). The coil windings for each of the curvilinear fields can be driven with currents up to 80 A and can be ramped to this field inside 200 μs (8,9). The additional gradient coils were driven using a custom setup, which utilizes an array of Advanced Measurement Control (AMC) processors present in the Siemens architecture for parallel RF transmit applications. Each of the eight AMC processors has a separate parallel RF transmit channel. Additionally, each AMC processor contains the digital signal processors to drive a set of three gradient channels, which when set up for parallel RF transmit are not normally utilized (16). Our present arrangement uses a "Master" host computer to control the linear gradient channels and the RF transmit and receive as normal, with a networked "Slave" computer driving the two additional curvilinear encoding fields using an additional set of high-performance gradient amplifiers (capable of 625 A and 2 kV per channel). Using this setup, it is possible to compose pulse sequences which synchronously drive the five available gradients simultaneously and independently. An integrated RF head coil (Siemens) was fitted inside the gradient insert coil and consisted of a single-channel transmit/receive RF coil surrounding an eight-channel receive-only RF coil.

Experiments

Experiments were performed using each of the six trajectories described above. All Cartesian trajectories could be acquired using a standard gradient-recalled echo (GRE) sequence. The 4D-RIO trajectory, however, includes a discontinuity in the middle of each read-out line, where the (k_x,k_y) component of the *k*-vector needs to jump from one side of the (k_x,k_y)-space to the opposite side. To achieve this experimentally, we decided to split the readout into

two halves, allowing time for the linear gradients to sweep from one side of the (k_x,k_y)-space to the other. Meanwhile, the PatLoc encoding fields need only a small lobe to counteract the moment accrued during the additional ramps. We appreciate that such drastic splitting of the readout may lead to complications in calculating the expected image contrast, but decided to treat this experiment as a "proof-of-principle" that the 4D encoding is experimentally feasible. A pulse sequence diagram for each of the six trajectories is shown in Fig. 3 (although a separate plot is not shown for the 4D-RIO^2 trajectory as the diagram would be identical to the 4D-RIO trajectory—they differ only in the relative angle of advance between the spokes).

All acquisitions were matched to 128 × 128 samples, slice thickness of 5 mm (slice selection always performed using linear *z*-gradient), and a FoV of 252 mm. For the PatLoc encoding fields, the FoV was matched by scaling the field such that one step in k_a or k_b resulted in a phase accrual of π radians at 126 mm from the isocenter. The TR was 500 msec for all measurements, leading to a scan-time of 64 sec for each acquisition. The same phantom was used for all measurements—a 190-mm-diameter cylinder containing many Plexiglas tubes parallel to the long-axis of the cylinder to provide structure, filled with water doped with nickel sulfate and sodium chloride.

The reconstruction of the 4D-RIO data requires sensitivity maps for each of the eight channels of the RF receive coil. These were generated from a separate 256 × 256 GRE, 5 mm thickness, 220 mm FoV, acquisition using only the linear gradients, where the sensitivity maps were estimated using the adaptive method described in (17). Maps of each of the PatLoc encoding fields were obtained by using a custom multiecho GRE sequence (128 × 128 GRE, 5 mm thickness, 220 mm FoV) which blips the PatLoc fields before each of the last 4 echoes of an 8 echo acquisition, using multiple echoes to increase SNR. The phase accrual due to a known gradient area for each of the PatLoc fields was then approximated by a fitted quadratic surface to allow smooth extrapolation beyond the object boundaries.

Reconstruction of the data was performed using the CG method described above onto a 160 × 160 Cartesian grid. As the encoding matrix, **E**, was too large to fit in the computer's working memory, the slower line-by-line implementation was used. Fifteen iterations were performed, each taking ~3 min, to reconstruct the data from each trajectory.

Preliminary experiments had indicated a strong sensitivity of the reconstruction of the 4D-RIO data to the precise knowledge of the alignment of the PatLoc fields with respect to the linear gradients. To calibrate for small errors in the estimation of the fields, the 4D-RIO sequence was repeated twice further, once playing only the linear gradients and once playing only the PatLoc encoding fields. Each of these datasets alone is sufficient to reconstruct an image of the object, but the PatLoc encoded data will lead to differing spatial resolution across the object. By reconstructing only a subset of the acquired data (64 × 32 datapoints instead of 128 × 128 acquired, four RF coils instead of eight acquired) onto a smaller grid (100 × 100 instead of 160 × 160), the reconstruction time was reduced to 2.5 min in total. This was sufficiently short to allow an optimization of the alignment of the linear-encoded image and the PatLoc-encoded image. An eight parameter optimization was performed, varying the magnitude, rotation angle, and saddle center offset (in *x* and *y*) for both PatLoc fields. The least-squares difference between the magnitude of the two images within a mask containing just the object was used as the cost function in the optimization procedure, which was performed using a trust-region-reflective algorithm (as implemented by the Matlab function "lsqcurvefit").

RESULTS

Simulations and Local *k*-Space

Pure Linear Cartesian

The most trivial example of the local *k*-space representation is the Pure Linear Cartesian trajectory. Whenever there is only linear encoding present, the local *k*-space will be identical to the conventional *k*-space at all locations **x**. This is shown in Fig. 4a, along with the reconstructed image. As would be expected, the apparent resolution is uniform across the entire object.

Pure PatLoc Cartesian

The local *k*-space grid and reconstructed image for the Pure PatLoc Cartesian trajectory are shown in Fig. 4b. This trajectory corresponds to the experiments described in Schultz et al., where it was shown that the resulting image resolution is higher at the edges than in the center of the FoV (3). Figure 4b shows a large coverage of the local *k*-space in the plots at the edge of the FoV, corresponding to the observed high resolution at the edges of the reconstructed image. Toward the center of the FoV, the coverage of the local *k*-space gets smaller and smaller, collapsing to a single point at the very center. At this very central point—the saddle-point of the quadratic SEMs—there is effectively no spatial encoding as, locally, the spins are all in phase throughout the readout. The corresponding reduction of resolution toward the center of the FoV is clearly visible in the reconstructed image.

Dual Cartesian

The local *k*-space grid for the Dual Cartesian trajectory shown in Fig. 4c is similar in appearance to that of the Pure PatLoc Cartesian trajectory in Fig. 4b but appears to have been shifted to the left of the FoV. This is confirmed by the reconstructed image, where the lower-resolution region has also been shifted to the left. A simple explanation for the origin of this shift can be found by considering the shape of the net encoding field. From the Appendix, we can see that the net field produced by the linear and quadratic encoding fields will always maintain the shape of a hyperbolic paraboloid, but the saddle point can be shifted in the *x* or *y* directions (with a global offset). The Appendix shows that the normalized coordinates of the center of the saddle (x_c,x_c) can be written as an expression of the four components of the *k*-vector:

$$x_c = \frac{-k_a k_x - k_b k_y}{2(k_a^2 + k_b^2)} \quad [7]$$

$$y_c = \frac{k_a k_y - k_b k_x}{2(k_a^2 + k_b^2)} \quad [8]$$

When both the linear and the PatLoc encoding fields are following the same trajectory (i.e., $k_x = k_a$, $k_y = k_b$), then we can see from Eqs. 7 and 8 that the coordinates of the saddle point of the net phase encoding will be fixed at $(x_c,y_c) = (-0.5,0)$, independent of the actual trajectory chosen. This means that the effect of the encoding using the Dual Cartesian trajectory is identical to that of using the Pure PatLoc Cartesian trajectory—but with the center of the PatLoc fields shifted to the new coordinates $(-0.5,0)$. It should be noted that, besides this spatial offset, the actual phase encoding will not be identical due to the constant offset term (the constant C in Eq. A2). However, because this extra phase offset term is identical at all spatial positions $\mathbf{x}$, it will not alter the properties of the inversion of Eq. 3.

Toward the right of the object, where from the local k-space we would expect the resolution to be high, it is also noticeable that some image degradation occurs. This appears to be caused by an insufficient number of iterations used in the CG reconstruction to accurately resolve this region. This artifact can be resolved by increasing the number of CG iterations used from 50 to 100 (see Discussion and Fig. 9).

Dual Swapped Cartesian

The local k-space grid for the Dual Swapped Cartesian trajectory shown in Fig. 4d is markedly different to those of the previously considered trajectories, demonstrating individual plots which are strongly asymmetric. The asymmetries of the local k-space also correspond to visibly asymmetric resolution in the reconstructed image. The origin of these strikingly different properties can again be identified by considering the path followed by the saddle point of the net encoding field during the readout. If we set $k_x = k_b$ and $k_y = k_a$ in Eqs. 7 and 8, we find that the radius of the saddle center coordinates is now a constant, $\sqrt{x_c^2 + y_c^2} = 0.5$, regardless of the actual trajectories followed. Figure 6a,b shows the location of the saddle center during the Dual Cartesian and the Dual Swapped Cartesian trajectories. In Fig. 6a, we see the fixed saddle center coordinates of $(-0.5,0)$ throughout the entire readout, and in Fig. 6b, we see that the saddle center is constrained to a circle at a fixed radius of 0.5 from the FoV center.

4D-RIO

As can be seen from Fig. 5a, the 4D-RIO trajectory results in a local k-space distribution which shares the basic property of the Pure PatLoc Cartesian trajectory—higher coverage at the edges than at the center of the FoV. However, the 4D-RIO trajectory retains a finite level of coverage across the entire FoV, never collapsing to a single point as in the case of the Pure PatLoc Cartesian or Dual Cartesian trajectories. The reconstructed image demonstrates that the resolution is sufficient across the FoV to be able to resolve the checkerboard pattern on the digital phantom. The path followed by the saddle center of the net encoding field during the readout is shown in Fig. 6c, where it can be seen to follow a star-like pattern.

4D-RIO^2

The modified version of 4D-RIO with $\Delta\theta_{\mathrm{Lin}} = -2\Delta\theta_{\mathrm{Pat}}$ results in quite a different local k-space pattern to the 4D-RIO trajectory, as shown in Fig. 5b. Overall the extent of the coverage is very similar, but the local k-space plots for the top half of the FoV do not cover the local k-space center. Correspondingly, the reconstructed image shows very little signal in the top half of the FoV where it appears that only the higher spatial frequencies are reconstructed. This broken symmetry with respect to the completeness of the local k-space coverage arises because during the entire readout the saddle center of the net encoding sweeps only through the bottom half of the FoV, as shown in Fig. 6d.

Experimental Results

Figure 7a–f shows the reconstruction of the experimental data for each of the six trajectories examined in this article. The images from the experiments are in very good agreement with the simulations (Figs. 4 and 5), with the main visual differences (i.e., the noticeable differences in symmetry for the Dual Cartesian and the 4D-RIO^2 trajectories) explainable by the fact that the experimental PatLoc insert coil generates fields rotated by $\sim 22.5^\circ$ from those used in simulation. The quadratic fields were chosen to be aligned with the axes for the simulations to keep the descriptions clearer and the algebra shown in the Appendix easier to follow—but it can be extended to the more general case of arbitrarily rotated encoding fields.

To demonstrate the effectiveness of the calibration of the alignment of the linear and the quadratic fields (as described in the section Methods: Experiment), Fig. 8a shows the reconstruction of the same 4D-RIO data as Fig. 8b but without the offsets included. A large difference in the quality of the reconstructed image is observable, despite the small magnitude of the offsets, which were found to be no larger than 0.5% for the magnitude, 1.6 mm for the spatial offset and 0.15° for the angle of rotation.

DISCUSSION

We have successfully demonstrated that spatial encoding in MRI can be taken far beyond the "traditional" approach of only using linear gradients, and of using only two encoding fields to encode a two-dimensional image. We introduced the concept of a local k-space which allows some of our established intuition for properties of an encoding trajectory to be extended into this new encoding environment. Through simulations in conjunction with the local k-space, we were able to develop a novel 4D encoding trajectory we refer to as 4D-RIO which results in the variable spatial resolution across the object, as with pure quadratic PatLoc encoding, but retains useful resolution at the isocenter where pure quadratic encoding cannot. We implemented a custom hardware setup capable of driving, simultaneously to the linear x,y, and z

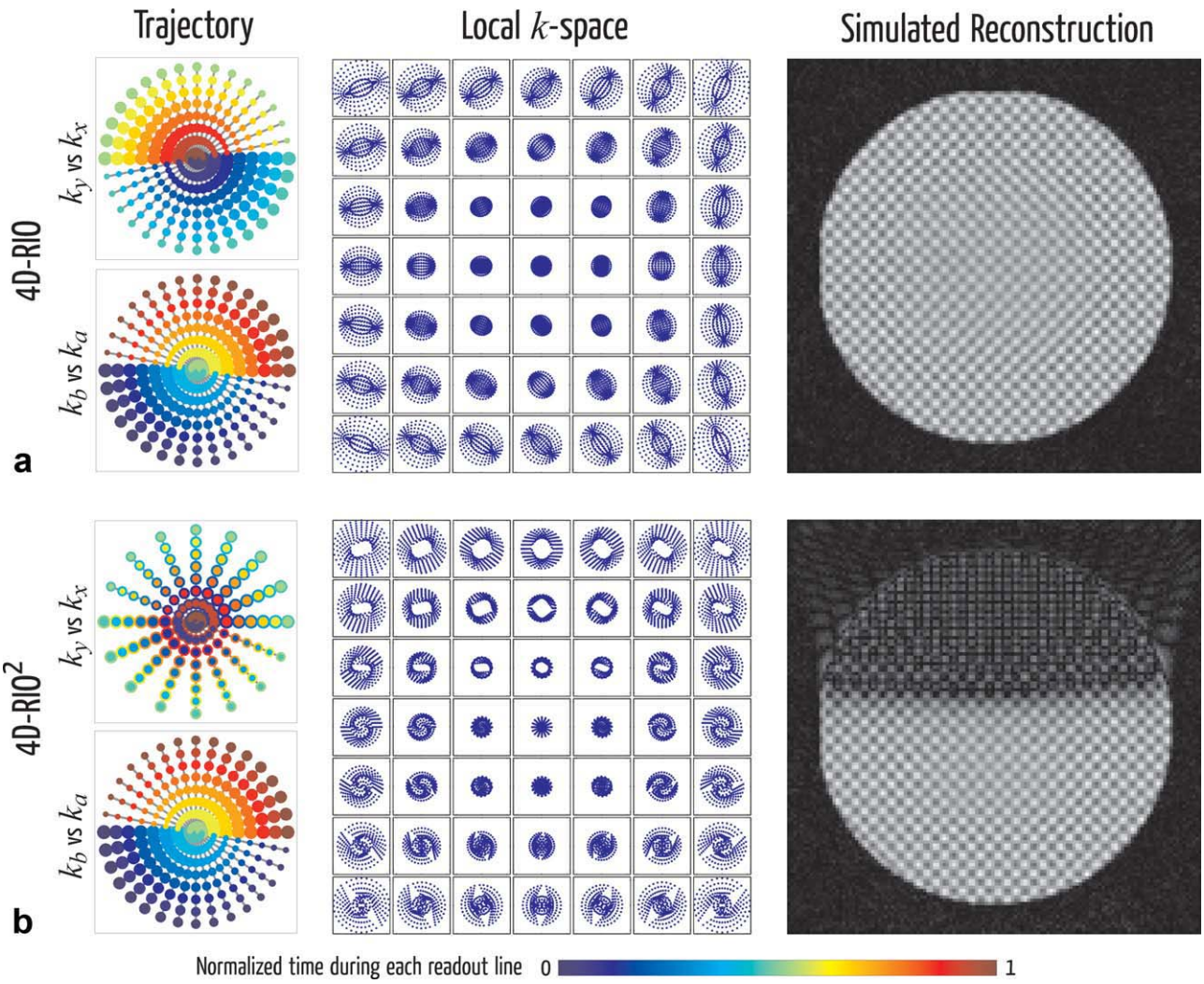

FIG. 5. Trajectory diagrams, 7 × 7 grid local *k*-space diagrams and reconstructed simulated data for (**a**) 4D-RIO trajectory (with $\Delta\theta_{Lin} = \Delta\theta_{Pat}$) and (**b**) 4D-RIO^2 trajectory (with $\Delta\theta_{Lin} = -2\Delta\theta_{Pat}$). Size and colors of circles in trajectory diagrams follow Fig. 4. It should be noted that to implement these trajectories experimentally, it was necessary to split the readout into two to achieve the large jump in the k_x,k_y-space. [Color figure can be viewed in the online issue, which is available at wileyonlinelibrary.com.]

gradients, the two additional quadratic encoding fields offered by a custom-built gradient insert coil, also with high performance amplifiers. We were then able to demonstrate the 4D-RIO sequence experimentally, obtaining images in good agreement with the simulations.

Designing New Trajectories

It is not immediately clear what 4D encoding trajectory should be chosen for reconstructing a 2D image, i.e., how the linear and PatLoc encoding fields should be combined to optimally encode the image. The linear gradients are orthogonal to each other, and the two quadratic PatLoc encoding fields used here are also orthogonal to each other. However, the linear encoding fields are not orthogonal to the quadratic encoding fields, meaning that care needs to be taken in designing combined 4D trajectories to ensure that good encoding is achieved where it is desired. We found that the concept of a local *k*-space was useful for comparing candidate encoding trajectories, allowing insight to help both understand the results from simulations and experiments as well as predicting the behavior of new trajectories prior to their implementation.

The 4D-RIO trajectory presented here is a first example of a novel trajectory which results in a good coverage of the local *k*-space across the entire FoV. The trajectory was developed following the observation from simulations of a 1D object (data not shown) that good reconstructions were achieved using trajectories which never allow the whole FoV to be refocused simultaneously (i.e., the condition $|\mathbf{k}_{Lin}| = |\mathbf{k}_{Pat}| = 0$ is never reached). Trajectories designed in this way have the unusual property that in order for a particular region to be refocused (i.e., to acquire the center of the local *k*-space) then the center of the saddle of the net encoding field needs to pass through that region at some point during the readout. As shown by the 4D-RIO^2 trajectory, if one region is avoided by the saddle center, then the image cannot be reconstructed in that region. Trajectories can easily be designed which make the saddle center follow arbitrary paths

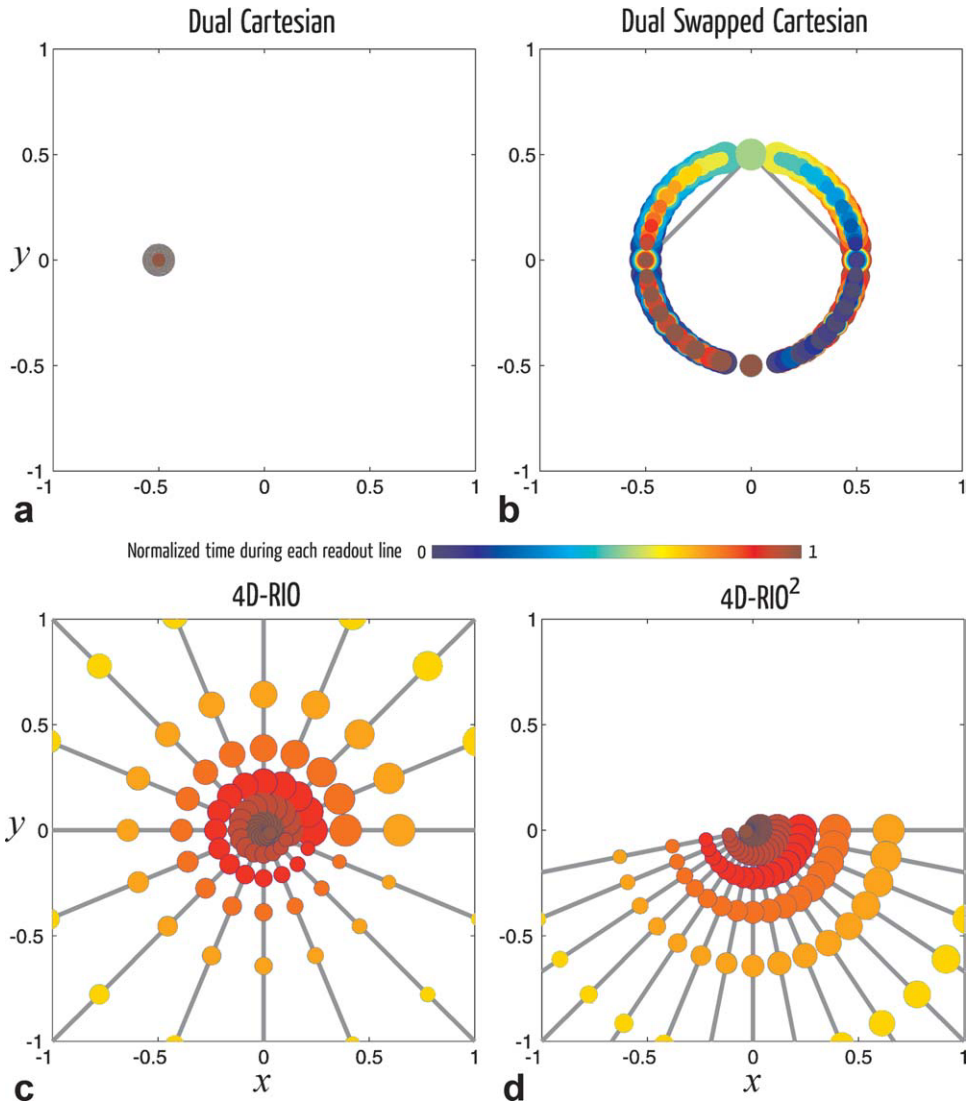

FIG. 6. When using simultaneous linear and quadratic spatial encoding the center of the saddle of the quadratic field is spatially displaced by the linear fields. This figure shows the (x,y) coordinates (normalized from -1 to $+1$ across the FoV) for the position of the saddle center during (**a**) Dual Cartesian, (**b**) Dual Swapped Cartesian, (**c**) 4D-RIO, and (**d**) 4D-RIO^2 trajectories. Size and colors of circles follow Fig. 4. For (b–d), the saddle center moves during each readout line, as well as between readout lines. [Color figure can be viewed in the online issue, which is available at wileyonlinelibrary.com.]

through the object. This effect allows a kind of inner-volume imaging—where instead of selecting the area of interest by selective excitation (eg. using 2D RF pulses (18) or nonlinear fields as slice-select gradients (19)) the selection of signal is performed by selective refocusing. This may be an interesting line of investigation for future work.

An observation which may be of use for the design of new trajectories is that at the center of the FoV the quadratic encoding fields have no effect, so the local k-space at the FoV center is necessarily identical to the trajectory followed by the linear gradients in (k_x,k_y)-space. This is easily confirmed by comparing the trajectory in (k_x,k_y)-space with the center tile of the local k-space grid for each of the trajectories shown in Figs. 4 and 5.

Number of CG Iterations

Whenever an iterative approach such as CG is used, it is necessary to choose an appropriate number of iterations. In the case of the reconstruction method presented here, it is important to not set this number too high, as the inherent regularization of the CG method is exploited through keeping the number low. In the case of the Dual Cartesian trajectory, the simulated data showed image degradation toward the right of the FoV after 50 iterations (Fig. 4c), which can be resolved by increasing the number of iterations to 100 (Fig. 9a,b). Clearly, some trajectories require more iterations than others to reach the optimal reconstruction, so care should be taken when comparing reconstructed images that a suitable choice has been made.

It should be noted that although increasing the number of iterations does also slightly increase the amount of signal in the top half of the FoV using the 4D-RIO^2 trajectory, the low-frequency information is clearly still not recovered due to the lack of coverage of the center of the local k-space in this region (Fig. 9c,d).

Sensitivity to Calibration

The demonstration that the reconstructed image is so sensitive to such minor offsets in the PatLoc field used for reconstruction might be a cause for concern. However, even with pure linear encoding, radial acquisition trajectories are known to be highly sensitive to B0 inhomogeneity, gradient delays, and gradient nonlinearities (20,21). As the delays and nonlinearities are highly reproducible on a particular system, a detailed calibration should only

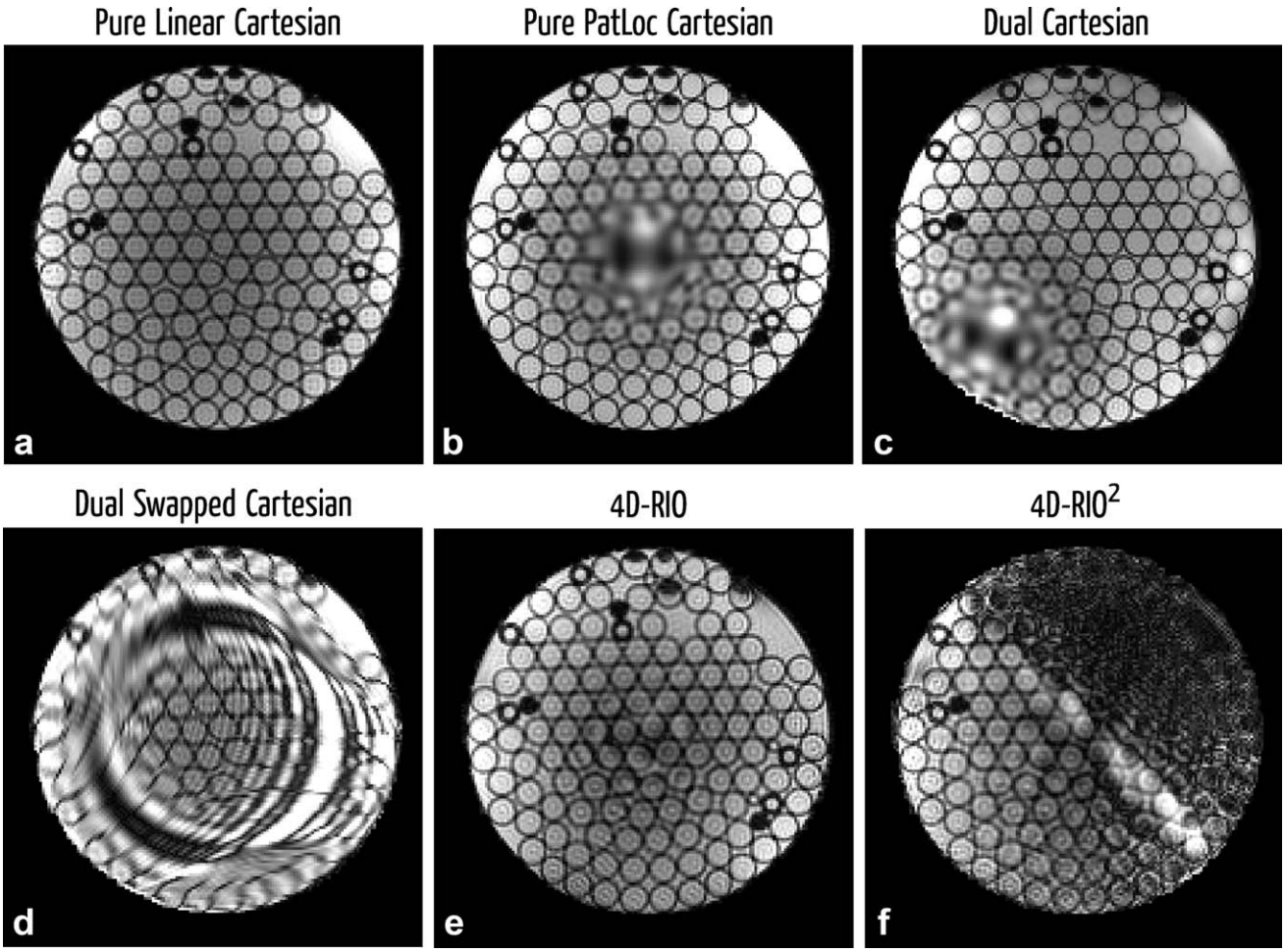

FIG. 7. Reconstructed images from experimental data acquired using (**a**) Pure Linear Cartesian, (**b**) Pure PatLoc Cartesian, (**c**) Dual Cartesian, (**d**) Dual Swapped Cartesian, (**e**) 4D-RIO, and (**f**) 4D-RIO^2 trajectories. All images are reconstructed to a 160 $\times$ 160 grid.

need to be performed once. It should be noted that these calibrations were of the encoding fields themselves, rather than the trajectory (although the way the correction was performed it may also be able to correct some trajectory errors) and so, in principle, single-shot acquisitions with 4D-RIO-like trajectories should also be achievable.

If desired, the B0 inhomogeneities can be included in the iterative method of image reconstruction, as a separate B0 map along with the timing of the readout can be incorporated into the encoding matrix. For the cylindrical phantom used here, the shimming was found to be good enough to see no appreciable benefit when this was included.

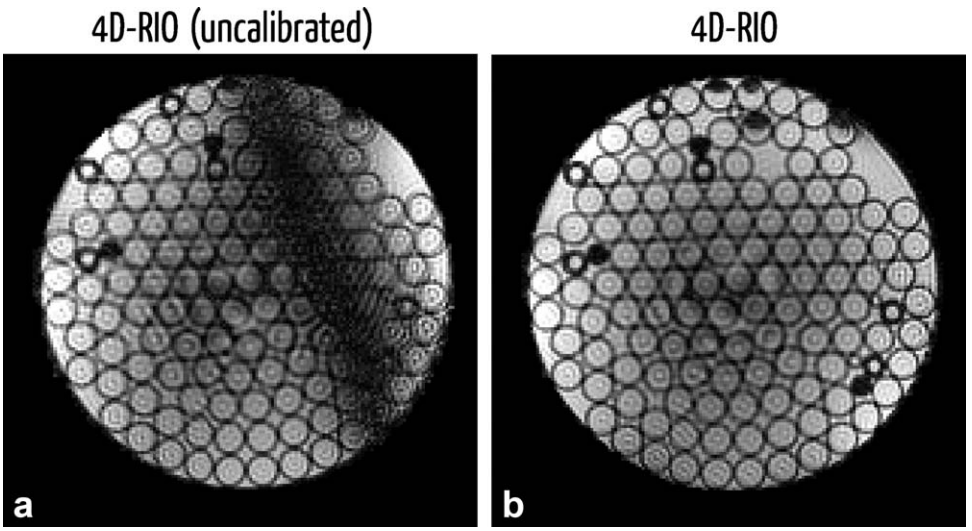

FIG. 8. The effect of the calibration of the alignment of the PatLoc and linear encoding fields as described in the text. **a**: 4D-RIO reconstruction before calibration, (**b**) reconstruction of the same data following calibration. All images are reconstructed to a 160 $\times$ 160 grid.

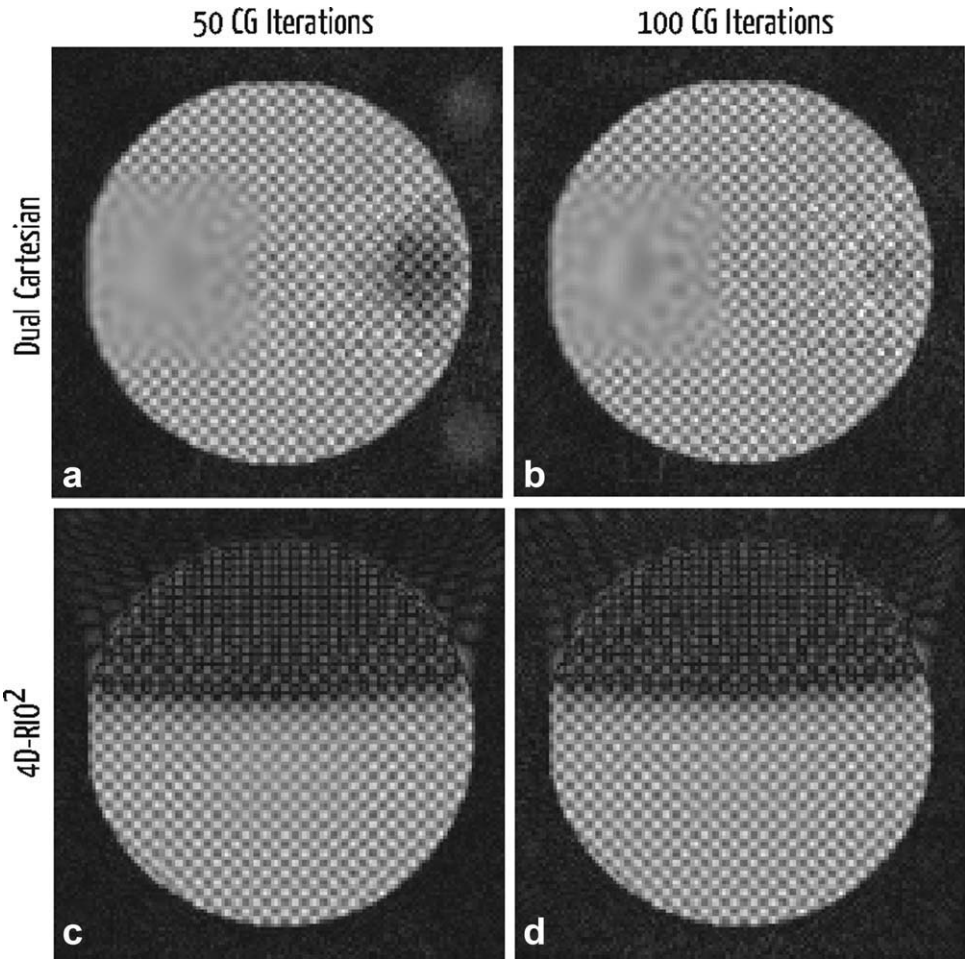

FIG. 9. Comparing the effect of the number of CG iterations on the reconstruction of simulated data. Dual Cartesian data are shown reconstructed using (**a**) 50 and (**b**) 100 iterations. After 100 iterations, the image degradation toward the right of the FoV in (a) is no longer observed. For the 4D-RIO^2 trajectory, increasing the number of CG iterations from (**c**) 50 to (**d**) 100 results in only a small increase in the resolved signal in the top half of the FoV.

Image Contrast

The 4D-RIO trajectory presented here may exhibit unusual image contrast—there is no single time when all spins are refocused (as in conventional imaging when acquiring the center of *k*-space) so there is no time which can be considered the unique "effective TE" for the whole slice. The long delay used here between the two halves of each readout line will further emphasize this difference in effective TE. The phantom used was homogeneous in terms of T1 and T2, so contrast variations were not observed. Further investigation into the true contrast properties of such 4D trajectories will be the focus of future work.

Generalized Encoding

In this work, we have focused on quadratic fields as these match the hardware we currently have available. However, the ideas introduced here can be applied to reduce trajectories using an arbitrary number of arbitrary encoding fields down to a set of local *k*-space plots which can be interpreted similarly to conventional *k*-space diagrams. This may be of particular relevance when attempting to find optimal encoding strategies using novel technologies such as an array of individually controllable encoding coils (22). It has been suggested that nonlinear encoding fields may deliberately be designed to complement RF coil sensitivity profiles to optimize parallel imaging acceleration (23). How best to formulate this optimization, however, remains an open question. If RF coil profiles are included in the local *k*-space representation, then a separate set of local *k*-space plots would be required for each RF coil. Each individual local *k*-space plot will be offset in the (k_x,k_y)-plane according to the local spatial derivative of the phase of the RF coil profile at the corresponding spatial location. It may be possible to use this property to help with the design of nonlinear encoding fields which might favorably combine with the RF coil profiles. However, this would only make use of the phase information of the RF coil profiles. It is difficult to envisage how the magnitude of the RF coil profiles might also be incorporated. Ultimately, one might expect that the optimal multidimensional encoding trajectory is the one where the inversion of the encoding matrix is as well conditioned as possible for a given readout duration (the familiar concept of "undersampling" becomes difficult to define as there is no longer a clear definition of "fully sampled"). However, in general, this requires simultaneous optimization of the encoding fields and the trajectory along which they would be driven.

Future work

Although the local *k*-space plots suggest that the 4D-RIO sequence should have resolution which is at least as good as the Pure Linear Cartesian trajectory across the

entire FoV, the 4D-RIO image has some loss of image quality towards the center (Fig. 7a vs Fig 7e). However, we expect that more careful calibration of our hardware (for example, the eddy-current compensation has not yet been adjusted for the PatLoc coils) and the trajectories should improve these minor residual artifacts. An obvious disadvantage of these methods is the longer reconstruction time compared to Fourier imaging. We expect future work to be able to overcome this as the reconstruction is well suited to computational parallelization using either multi-processor CPUs or graphics cards. We are also now in the process of testing these methods in vivo, having recently obtained internal review board approval for human imaging.

ACKNOWLEDGMENTS

The authors would like to thank Feng Jia from the University of Freiburg Department of Microsystems Engineering for his work on the coil winding design, Bruker France (Bruker BioSpin S.A.) and Frederic Jaspard for helping to manufacture the gradient coil with the technology available in Wissembourg and Dr. Walter RT Witschey for additional pulse sequence development and considerable assistance in compiling the manuscript.

APPENDIX

Algebraic Representation of the Addition of 2D Linear and Quadratic Fields

If $\psi_a(\mathbf{x})$ x^2 y^2 and $\psi_b(\mathbf{x})$ $2xy$, we can create a net phase distribution, $\phi(\mathbf{x})$, in combination with the linear gradients:

$$\phi(\mathbf{x}) = k_x x + k_y y + k_a(x^2 - y^2) + k_b(2xy) \qquad [A1]$$

where k_x,k_y,k_a and k_b are the normalized components of the 4D k-vector and x and y are normalized from -1 to $+1$ across the FoV.

By introducing new variables, we can also choose to write $\phi(\mathbf{x})$ in the form:

$$\phi(\mathbf{x}) = k_a\left((x - x_c)^2 - (y - y_c)^2\right) + k_b(2(x - x_c)(y - y_c)) + C \qquad [A2]$$

where x_c and y_c are the coordinates of the new center (or saddle point) of the saddle and C is a constant.

Multiplying out and term-matching gives:

$$\phi(\mathbf{x}) = x(-2k_a x_c - 2k_b y_c) + y(2k_a y_c - 2k_b x_c) + k_a(x^2 - y^2) + k_b(2xy) + k_a(x_c^2 - y_c^2) + 2k_b x_c y_c \qquad [A3]$$

Therefore, by comparing (A1) and (A3):

$$k_x = -2k_a x_c - 2k_b y_c \qquad [A4]$$

$$k_y = 2k_a y_c - 2k_b x_c \qquad [A5]$$

$$C = -k_a(x_c^2 - y_c^2) - 2k_b x_c y_c \qquad [A6]$$

These equations can then be rearranged to give x_c and y_c in terms of the components of the k-vector:

From (A5):

$$y_c = \frac{2k_a x_c + k_y}{2k_a} \qquad [A7]$$

(A7)→ (A5):

$$k_x = -2k_a x_c - \frac{2k_b(2k_b x_c + k_y)}{2k_a} \qquad [A8]$$

$$k_a k_x = -2k_a^2 x_c - 2k_b^2 x_c - k_b k_y \qquad [A9]$$

$$x_c = \frac{-k_a k_x - k_b k_y}{2(k_a^2 + k_b^2)} \qquad [A10]$$

Analogously for y_c

$$y_c = \frac{k_a k_y - k_b k_x}{2(k_a^2 + k_b^2)} \qquad [A11]$$

REFERENCES

1. Parker DL, Hadley JR. Multiple-region gradient arrays for extended field of view, increased performance, and reduced nerve stimulation in magnetic resonance imaging. Magn Reson Med 2006;56:1251–1260.
2. Hennig J, Welz AM, Schultz G, Korvink J, Liu Z, Speck O, Zaitsev M. Parallel imaging in non-bijective, curvilinear magnetic field gradients: a concept study. Magma 2008;21:5–14.
3. Schultz G, Ullman P, Lehr H, Welz AM, Hennig J, Zaitsev M. Reconstruction of MRI data encoded with arbitrarily shaped, curvilinear, non-bijective magnetic fields. Magn Reson Med 2010;64:1396–1409.
4. Wedeen VJ, Chao YS, Ackerman JL. Dynamic range compression in MRI by means of a nonlinear gradient pulse. Magn Reson Med 1988; 6:287–295.
5. Maudsley AA. Dynamic range improvement in NMR imaging using phase scrambling. J Mag Res 1988;76:287–305.
6. Yamada Y, Tanaka K, Zenmon A. NMR Fresnel transform imaging technique using a quadratic nonlinear field gradient. Rev Sci Instrum 1992;63:5348–5358.
7. Stockmann JP, Ciris PA, Galiana G, Tam L, Constable RT. O-Space imaging: highly efficient parallel imaging using second-order nonlinear fields as encoding gradients with no phase encoding. Magn Reson Med 2010;64:447–456.
8. Welz AM, Cocosco C, Dewdney A, Schmidt H, Jia F, Korvink J, Hennig J, Zaitsev M. PatLoc gradient insert coil for human imaging at 3T. Proceedings of the ESMRMB, Antalya 2009. p 316.
9. Cocosco CA, Dewdney AJ, Dietz P, Semmler M, Welz AM, Gallichan D, Weber H, Schultz G, Hennig J, Zaitsev M. Safety considerations for a PatLoc gradient insert coil for human head imaging. Proceedings of the ISMRM 18th Scientific Meeting and Exhibition, Stockholm 2010. p 3946.
10. Bernstein MA, King KF, Zhou XJ. Handbook of MRI pulse sequences. Burlington, MA: Elsevier Academic Press; 2004.
11. Yang Y, Gu H, Zhan W, Xu S, Silbersweig DA, Stern E. Simultaneous perfusion and BOLD imaging using reverse spiral scanning at 3T: characterization of functional contrast and susceptibility artifacts. Magn Reson Med 2002;48:278–289.
12. Noll D. Rapid MR image acquisition in the presence of background gradients. Proceedings of the IEEE International Symposium on Biomedical Imaging, Washington DC, 2002.pp 725–728.
13. Deichmann R, Josephs O, Hutton C, Corfield DR, Turner R. Compensation of susceptibility-induced BOLD sensitivity losses in echo-planar fMRI imaging. NeuroImage 2002;15:120–135.
14. Pruessmann KP, Weiger M, Bornert P, Boesiger P. Advances in sensitivity encoding with arbitrary k-space trajectories. Magn Reson Med 2001;46:638–651.
15. Hansen PC. REGULARIZATION TOOLS: a Matlab package for analysis and solution of discrete ill-posed problems. Numer Algorithms 1994;6:1–35.
16. Fontius U, Baumgartl R, Boettcher U, Doerfler G, Hebrank F, Fischer D, Jeschke H, Kannengiesser S, Kwapil G, Nerreter U, Nistler J, Pirkl G, Potthast A, Roell S, Schor S, Adelsteinson E, Adriany G, Alagappan V, Gagoski B, Setsompop K, Wald LL, Schmitt F. A flexible 8-channel RF transmit array system for parallel excitation.

Proceedings of the ISMRM 14th Scientific Meeting and Exhibition, Seattle 2006. p 127.
17. Walsh DO, Gmitro AF, Marcellin MW. Adaptive reconstruction of phased array MR imagery. Magn Reson Med 2000;43:682–690.
18. Pauly J, Nishimura D, Macovski A. A k-space analysis of small-tip-angle excitation. J Magn Reson (1969) 1989;81:43–56.
19. Lee SY, Cho ZH. Localized volume selection technique using an additional radial gradient coil. Magn Reson Med 1989;12:56–63.
20. Glover GH, Pauly JM. Projection reconstruction techniques for reduction of motion effects in MRI. Magn Reson Med 1992;28:275–289.
21. Peters DC, Derbyshire JA, McVeigh ER. Centering the projection reconstruction trajectory: reducing gradient delay errors. Magn Reson Med 2003;50:1–6.
22. Juchem C, Nixon TW, McIntyre S, Rothman DL, Graaf RA. Magnetic field modeling with a set of individual localized coils. J Magn Reson 2010;204:281–289.
23. Tam L, Stockmann JP, Constable RT. Null space imaging: a novel gradient encoding strategy for highly efficient parallel imaging. Proceedings of the ISMRM 18th Scientific Meeting and Exhibition, Stockholm, 2010. p 2868.